

# **Final Technical Report for Assessments of Bubble Dynamics Model and Influential Parameters in Microbubble Drag Reduction**

**Reporting Period: July 1, 2004 to December 31, 2005**

**Report Date: March 2006**

**Prepared Under**

**Award No: N00014-04-1-0717**

***Submitted to***

**Patrick Purtell  
Office of Naval Research  
Ballston Centre Tower One  
800 North Quincy Street  
Arlington, VA 22217-5660**

***Submitted by***

**Principal Investigator: P.V. Skudarnov  
Co-Principal Investigator: C. X. Lin  
Applied Research Center  
(formerly Hemispheric Center for Environmental Technology)  
Florida International University  
10555 West Flagler Street, EC 2100  
Miami, FL 33174  
Phone: (305) 348-2377  
Fax: (305) 348-6308  
E-mail: Peter.Skudarnov@arc.fiu.edu**

## Table Of Contents

---

Table Of Contents .....	i
List of Figures .....	ii
1.0 Executive Summary .....	1
2.0 Introduction.....	2
3.0 Numerical Model .....	3
3.1 Single Phase Model .....	3
3.2 Multiphase Model.....	10
4.0 Turbulence Intensity Effect.....	16
5.0 Free Stream Velocity Effect.....	18
6.0 Surface Roughness Effect .....	21
7.0 Comparison of Multiphase CFD model and DNS .....	23
8.0 Conclusions.....	29
9.0 Publications Stemming from this Research .....	29
Acknowledgement .....	29
Nomenclature .....	30
References .....	31

## List of Figures

---

Figure 1. Schematic diagram of the computational domain. ....	6
Figure 2. The 112 x 64 computational grid.....	6
Figure 3. The $y^+$ in the first cell off the wall along the flat plate (Wall 1 + Wall 2 + Wall3) for the case with $Q/U_\infty A = 0.01$ and $U_\infty = 10.9$ m/s. ....	7
Figure 4. Comparison of simulated boundary layer velocity profile with standard law of the wall curves. ....	8
Figure 5. Comparison of the computed integrated drag coefficient with the experimental data of Merkle and Deutsch (1992) and the numerical model of Kunz et al. (2003). 8	
Figure 6. Schematic diagram of the computational domain used for surface roughness effect studies. ....	9
Figure 7. Comparison of the computed integrated drag coefficient for smooth wall with the experimental data of Deutsch et al. (2003). ....	10
Figure 8. The computational domain used in the multiphase model. ....	13
Figure 9. The 120x120 grid used in the multiphase model. ....	14
Figure 10. Inlet velocity profile used in the multiphase model. ....	14
Figure 11. The $y^+$ in the first cell of the wall along the flat plate for the $C_v = 0.01$ multiphase model case. ....	15
Figure 12. Free stream turbulent intensity effect on the drag reduction for different gas injection flow rates.....	16
Figure 13. Free stream turbulent intensity effect on the drag reduction for different density ratios of injected gas and water ( $Q/U_\infty A = 0.02$ ).....	17
Figure 14. Free stream velocity effect on the drag reduction for different gas injection flow rates.....	19
Figure 15. Free stream velocity effect on the drag reduction for different density ratios of water and injected gas ( $Q/U_\infty A = 0.02$ ). ....	19
Figure 16. Comparison of numerical simulations with different free stream velocities with experimental data of Deutsch et al. (2003). ....	20
Figure 17. Surface roughness effect on the microbubble drag reduction. ....	21
Figure 18. Comparison of numerical simulations with experimental data of Deutsch et al. (2003): a) Smooth Surface; b) Fine Rough Surface; c) Medium Rough Surface; d) Fully Rough Surface. ....	22
Figure 19. Gas volume fraction profiles at $x = 182$ mm. ....	24
Figure 20. Comparison of gas volume fraction profiles for different boundary conditions of the multiphase model.....	24

Figure 21. Comparison of gas volume fraction profiles for different injected gas density in the multiphase model. ....	25
Figure 22. Microbubble effects on the Turbulent Kinetic Energy. ....	26
Figure 23. Comparison of the drag reduction predicted by the multiphase CFD and DNS models. ....	26
Figure 24. Comparison of the drag reduction predicted by the multiphase CFD model with gas volume fractions increased 3.7 times and DNS model. ....	27
Figure 25. Comparison of gas volume fraction profiles predicted by the multiphase CFD model with gas volume fractions increased 3.7 times and DNS model. ....	28

## 1.0 Executive Summary

---

During the course of this research effort computational parametric studies of the microbubble drag reduction phenomena were conducted. The effects of mixture density variation, free stream turbulence intensity, free stream velocity, and surface roughness on the microbubble drag reduction were studied using a single phase model based on Reynolds-averaged Navier-Stokes transport equations. Additionally, predictions of Eulerian multiphase model for microbubble laden flow were compared with Direct Numerical Simulation from the open literature.

Good agreement was achieved between the simulations with the single phase model and experimental data of Deutsch et al. (2003). This good agreement was observed for both free stream velocity as well as surface roughness effect studies. Increased free stream turbulence intensity was observed to result in lower drag reduction, and this effect was stronger for higher density ratios of water and injected gas. For the same free stream velocity increase, the drag reduction was higher for higher density ratio. For fixed gas injection rate, lower drag reduction was predict for higher free stream velocity, and increased drag reduction was obtained with increased surface roughness.

The drag reduction predicted by the multiphase model was substantially lower than that predicted by the Direct Numerical Simulation model of Ferrante and Elghobashi (2004). However, gas volume fraction and turbulent kinetic energy profiles predicted by the multiphase model were similar but not identical to those predicted by the DNS of Ferrante and Elghobashi (2004).

## 2.0 Introduction

---

An increase in range or speed of the U.S. Navy's surface vessels, submarines, underwater vehicles, and weapons can be achieved by reducing the skin friction drag of these objects. Microbubble drag reduction (MDR) is a unique flow control technique that employs injection of gas into a liquid turbulent boundary layer to form microbubbles that can dramatically reduce the skin friction drag. This technique, which is able to provide drag reductions of as much as 80%, offers great potential in Naval applications.

McCormick and Bhattacharya (1973) reported the first microbubble drag reduction experiments. During the past decades, many research efforts have been devoted to microbubble drag reduction (Merkle and Deutsch 1992). The work conducted by researchers in the former Soviet Union and in the United States, primarily by the Applied Research Laboratory (ARL) at The Pennsylvania State University, provided the benchmark in microbubble drag reduction research. It has been found that there are many factors that influence microbubble drag reduction, including air jet flow rate, injection process, free stream velocity, pore size, buoyancy, and surface configuration. As evidenced by published papers in the open literature, most of the previous studies of microbubble drag reduction were conducted experimentally. Due to the complexity of the microbubble boundary layers, theoretical investigations have fallen behind the progress made by experimental studies. It is recognized that a better understanding of the microbubble drag reduction mechanism is critical to its optimal performance with minimal use of gas volume in practical applications.

In recent years, analytical computational modeling of microbubble drag reduction has been attempted by several researchers (Madavan et al. 1985; Marie 1987; Kim and Cleaver 1995; Meng and Uhlman 1998; Xu et al. 2002; Kunz et al. 2003) to reveal the mechanism of the microbubble drag reduction phenomenon. A study by Legner (1984) proposed a simple stress model for gas bubble drag reduction and indicated that the drag reduction was caused by a combination of density reduction and turbulence modification. Meng and Uhlman (1998) suggested that bubble splitting was a plausible basic mechanism for reducing turbulence in a microbubble-laden turbulent boundary layer. These efforts made impressive progress toward the in-depth understanding of the mechanism from various angles. However, the available theoretical work is not sufficient to answer all the questions associated with microbubble drag reduction. The relative importance of postulated mechanisms remains unclear. One issue of specific interest is bubble breakup during microbubble drag reduction, which can give rise to turbulence attenuation. It has also been suggested that a simple density effect is the dominant source of drag reduction. Very recent experiments at ARL have also shown that significantly more drag reduction can be obtained on rough surfaces than on smooth surfaces with microbubble drag reduction. It is not understood why this phenomenon occurs.

In this project, the Applied Research Center (formerly Hemispheric Center for Environmental Technology) at Florida International University has conducted computational parametric studies of the microbubble drag reduction phenomena. The objective of this research was to assess the roles of mixture density variation, free stream turbulence intensity, free stream velocity, and surface roughness in microbubble drag reduction. Additionally, predictions of the open literature Direct Numerical Simulation for microbubble laden flow were compared with Eulerian multiphase model results.

### 3.0 Numerical Model

#### 3.1 SINGLE PHASE MODEL

During this project, computational assessment of the role of the mixture density, turbulence level, free stream velocity, and gas flow rate in the microbubble drag reduction was carried out. To perform this assessment, a two-dimensional computational fluid dynamics (CFD) model of microbubble-laden flow over a flat plate was developed. The model consisted of Reynolds-averaged Navier-Stokes (RANS) transport equations and a standard  $k$ - $\omega$  turbulence model (Wilcox 1998) with a low Reynolds number correction. This model was designed to be applied throughout the boundary layer when the near wall mesh is sufficiently fine. The RANS transport equations are

$$\frac{\partial \rho}{\partial t} + \frac{\partial}{\partial x_i} (\rho u_i) = 0 \quad (1)$$

$$\frac{\partial}{\partial t} (\rho u_i) + \frac{\partial}{\partial x_j} (\rho u_i u_j) = -\frac{\partial p}{\partial x_i} + \frac{\partial}{\partial x_j} \left[ \mu \left( \frac{\partial u_i}{\partial x_j} + \frac{\partial u_j}{\partial x_i} - \frac{2}{3} \delta_{ij} \frac{\partial u_l}{\partial x_l} \right) \right] + \frac{\partial}{\partial x_j} (-\rho \overline{u'_i u'_j}) \quad (2)$$

In the equations (1) and (2) as well as subsequent equations  $\rho$  and  $\mu$  are the mixture density and viscosity respectively, which are defined in (12) and (13) below. The last term in equation (2), called Reynolds stresses, is related to mean velocity gradients using Boussinesq hypothesis:

$$-\rho \overline{u'_i u'_j} = \mu_t \left( \frac{\partial u_i}{\partial x_j} + \frac{\partial u_j}{\partial x_i} \right) - \frac{2}{3} \left( \rho k + \mu_t \frac{\partial u_l}{\partial x_l} \right) \delta_{ij} \quad (3)$$

The transport equations for the turbulence kinetic energy  $k$  and the specific dissipation rate  $\omega$  are

$$\frac{\partial}{\partial t} (\rho k) + \frac{\partial}{\partial x_i} (\rho k u_i) = \frac{\partial}{\partial x_j} \left( \Gamma_k \frac{\partial k}{\partial x_j} \right) + G_k - Y_k \quad (4)$$

$$\frac{\partial}{\partial t} (\rho \omega) + \frac{\partial}{\partial x_i} (\rho \omega u_i) = \frac{\partial}{\partial x_j} \left( \Gamma_\omega \frac{\partial \omega}{\partial x_j} \right) + G_\omega - Y_\omega \quad (5)$$

where  $\Gamma_k$  and  $\Gamma_\omega$  are the effective diffusivity of  $k$  and  $\omega$ , respectively;

$G_k = \mu_t 2 S_{ij} S_{ij}$  (where  $S_{ij} = \frac{1}{2} \left( \frac{\partial u_j}{\partial x_i} + \frac{\partial u_i}{\partial x_j} \right)$ ) is the generation of turbulence kinetic energy

due to mean velocity gradients;  $G_\omega = \alpha \frac{\omega}{k} G_k$  is the generation of  $\omega$ , and  $Y_k = \rho \beta^* f_\beta k \omega$

and  $Y_\omega = \rho \beta f_\beta \omega^2$  are the dissipation of  $k$  and  $\omega$  due to turbulence.

The low Reynolds number correction is achieved by introducing damp coefficient  $\alpha^*$  into the turbulent viscosity equation as shown below (Wilcox, 1998):

$$\mu_t = \alpha^* \frac{\rho k}{\omega} \quad (6)$$

$$\alpha^* = \alpha_\infty^* \left( \frac{\alpha_0^* + \text{Re}_t / R_k}{1 + \text{Re}_t / R_k} \right) \quad (7)$$

where  $\alpha_\infty^* = 1$ ;  $\text{Re}_t = \frac{\rho k}{\mu \omega}$ ;  $R_k = 6$ ;  $\alpha_0^* = \frac{\beta_i}{3}$ ;  $\beta_i = 0.072$

The rest of the coefficients used in the above equations are defined as follows (Wilcox, 1998):

$$\alpha = \frac{\alpha_\infty}{\alpha^*} \left( \frac{\alpha_0 + \text{Re}_t / R_\omega}{1 + \text{Re}_t / R_\omega} \right), \quad \alpha_\infty = 0.52, \quad R_\omega = 2.95$$

$$\beta^* = \beta_\infty^* \left( \frac{4/15 + (\text{Re}_t / R_\beta)^4}{1 + (\text{Re}_t / R_\beta)^4} \right), \quad R_\beta = 8, \quad \beta_\infty^* = 0.09$$

$$f_{\beta^*} = \begin{cases} 1 & \chi_k \leq 0 \\ \frac{1+680\chi_k^2}{1+400\chi_k^2} & \chi_k \geq 0 \end{cases}, \quad \chi_k = \frac{1}{\omega^3} \frac{\partial k}{\partial x_j} \frac{\partial \omega}{\partial x_j}$$

$$\beta = 0.072, \quad f_\beta = \frac{1+70\chi_\omega}{1+80\chi_\omega}, \quad \chi_\omega = \left| \frac{\Omega_{ij}\Omega_{jk}S_{ki}}{(\beta_\infty^*\omega)^3} \right|, \quad \Omega_{ij} = \frac{1}{2} \left( \frac{\partial u_i}{\partial x_j} - \frac{\partial u_j}{\partial x_i} \right)$$

Wall boundary condition for the turbulence kinetic energy is

$$\frac{\partial k}{\partial n} = 0 \quad (8)$$

where  $n$  is the local coordinate normal to the wall.

Wall boundary condition for the specific dissipation rate is discussed in detail below, where the effect of surface roughness on microbubble drag reduction is addressed.

Mixture density variation due to microbubbles was modeled by introducing  $\text{CO}_2$  gas species and using the species transport model. In the species transport model, the local mass fraction of each species,  $Y_i$ , is predicted by solving a convection-diffusion equation for the  $i$ th species:

$$\frac{\partial}{\partial t} (\rho Y_i) + \nabla \cdot (\rho \bar{v} Y_i) = -\nabla \cdot \bar{J}_i + S_i \quad (9)$$



where  $\bar{J}_i$  is the diffusion flux of species  $i$  and  $S_i$  is the rate of creation from any sources. For turbulent flows such as those considered here, the diffusion flux has the following form:

$$\bar{J}_i = -\left(\rho D_{i,m} + \frac{\mu_t}{Sc_i}\right) \nabla Y_i \quad (10)$$

where  $Sc_i$  is the turbulent Schmidt number,  $\mu_t$  is the turbulent viscosity, and  $D_{i,m}$  is the diffusion coefficient for species  $i$  in the mixture.

The mixture density was computed using the volume-weighted mixing law:

$$\rho_m = \frac{1}{\sum_i \frac{Y_i}{\rho_i}} \quad (11)$$

The mixture viscosity was computed using the expression developed by Einstein (in Happel and Brenner, 1965):

$$\mu_m = \mu_l(1 + 2.5\phi) \quad (12)$$

where  $\mu_l$  is the viscosity of the liquid and  $\phi$  is the volumetric concentration of gas.

The CO<sub>2</sub> gas was introduced as species mass source in the first layer of cells along the porous section of the flat plate (“Wall 2” on Figure 1). Zero-gradient condition for all species was used on the flat plate. This model does not capture the physics of the microbubbles; however, it allows one to ascertain whether a simple mixture density variation effect is the dominant source of microbubble drag reduction. The model was solved using the FLUENT 6.2 CFD solver.

A 712 mm by 250 mm computational domain (Figure 1) with 112 x 64 grid (Figure 2) was used to solve the model. The height of the computational domain was selected so that it would be at least 20 turbulent boundary layer thicknesses, which, for the present case, was about  $\delta = 10$  mm. Wall-normal clustering of cells was used to resolve the boundary layer, and axial clustering was used near the ends of flat plate sections (Wall 1, Wall 2, and Wall3 in Figure 1). Dimensions of the computational domain and boundary conditions are shown schematically in Figure 1. Constant velocity boundary condition is used in the domain inlet, symmetry boundary conditions are used in the leading part of the domain as well as in the far field above the flat plate to simulate experimental water tunnel conditions, no slip boundary condition is applied at the flat plate, and constant pressure boundary condition is applied at the domain outlet. Values of  $k$  and  $\omega$  at the domain inlet were specified as  $1.2 \times 10^{-5} \text{ m}^2/\text{s}^2$  and  $1.2 \times 10^{-3} \text{ s}^{-1}$ , respectively. The same values were used as initial guesses for  $k$  and  $\omega$ . To compute gas inlet volumetric flow rates, the depth of the domain was assumed to be 102 mm. The dimensions of the domain corresponded to those of the Merkle-Deutsch (1992) flat plate experimental configuration to facilitate comparison of the results.

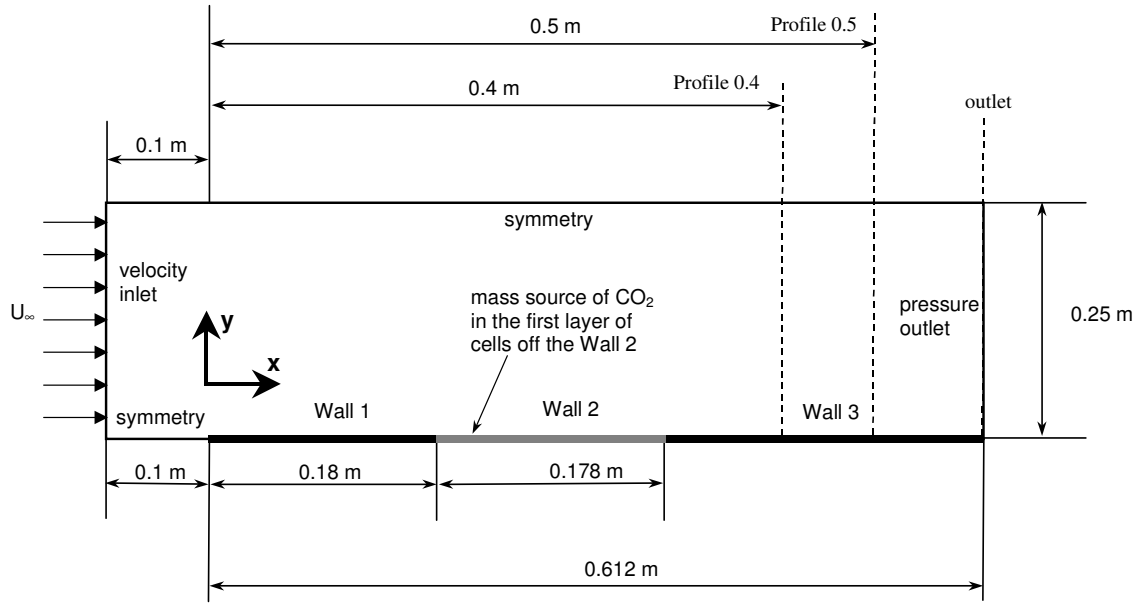


**Figure 1. Schematic diagram of the computational domain.**

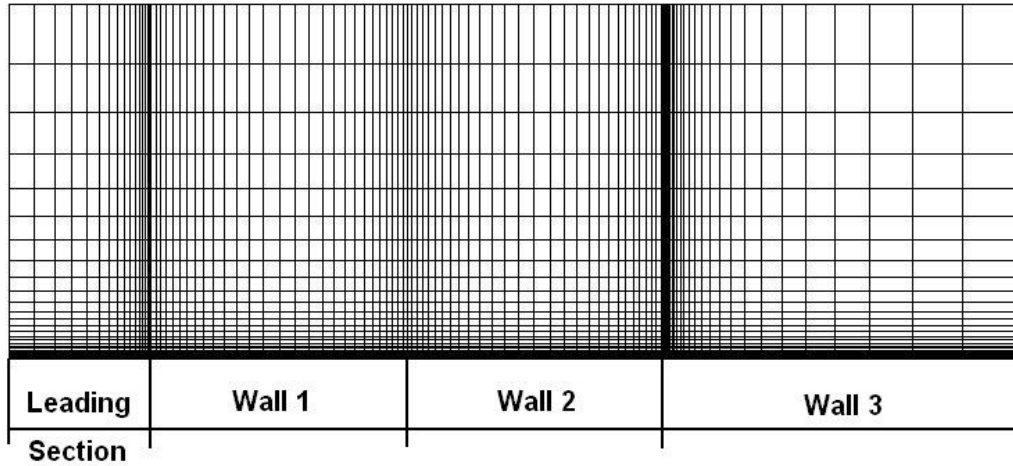


**Figure 2. The 112 x 64 computational grid.**

To validate that the computational grid satisfied  $y^+ \leq 1$  at the first cell off the wall, the  $y^+$  at the first cell was plotted along the flat plate for all computational cases. A sample plot for the case with  $Q/U_\infty A = 0.01$  and the free stream velocity of 10.9 m/s is shown in Figure 3. The  $y^+$  values along the flat plate for other studied cases had similar values and are not presented here.

In order to validate the model further, simulated boundary layer velocity profile for the case without gas injection was compared to standard law-of-the-wall curves. Boundary layer velocity profile in the outlet plain of the computational domain is plotted in Figure 4 in inner variables and compared to the standard curves. It is seen from the figure that the simulated profile is in good agreement with standard curves.

The ability of our model to predict the drag reduction is validated by comparing our model predictions with the experimental data of Merkle and Deutsch (1992) and with the ensemble averaged multifield two-fluid modeling results of Kunz et al. (2003). Figure 5 compares computed drag reduction (integrated drag coefficient over “Wall 3” flat plate section normalized by its single-phase value) for a number of nondimensional gas injection flow rates and several free stream velocities. The figure shows that not only the results of the current model are close to those of the more advanced model of Kunz et al. but also that the current model correctly predicts smaller drag reduction for lower free stream velocity as observed in the experiments. The results of our model are very close to those of Kunz et al. model, however, both models over predict experimentally observed drag reduction by as much as 50% in some cases.

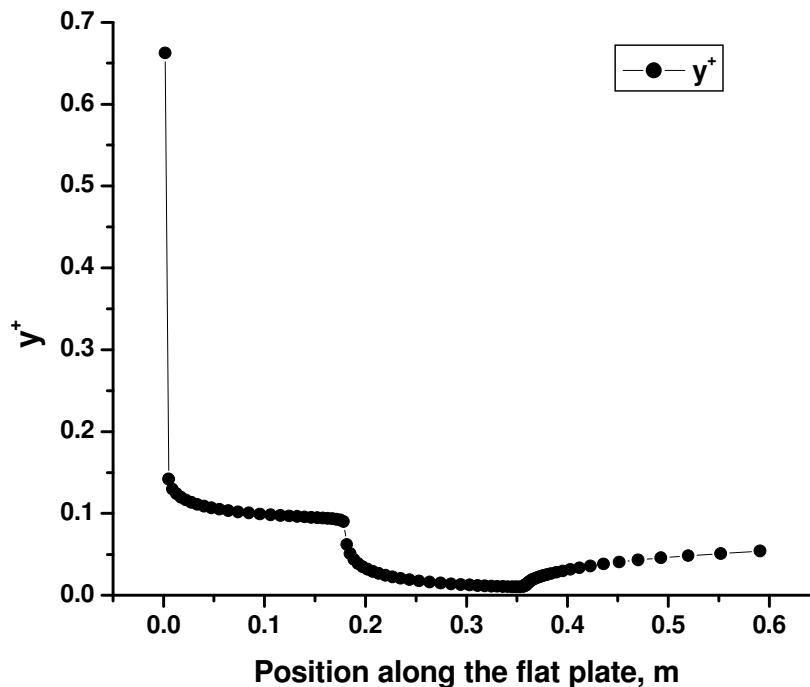


Figure 3. The  $y^+$  in the first cell off the wall along the flat plate (Wall 1 + Wall 2 + Wall3) for the case with  $Q/U_\infty A = 0.01$  and  $U_\infty = 10.9$  m/s.

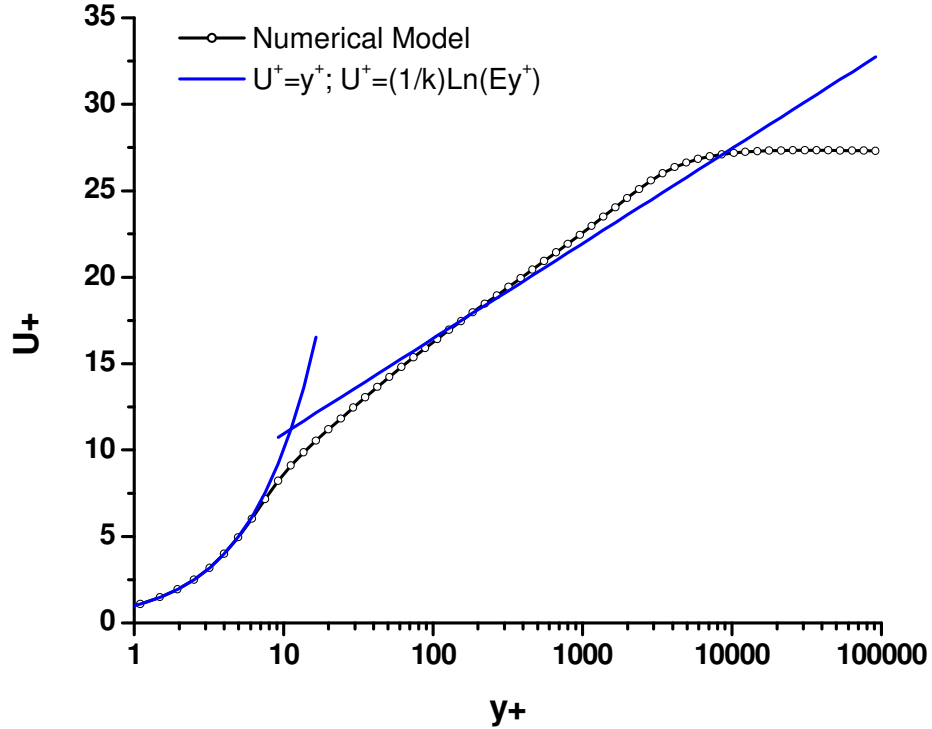


Figure 4. Comparison of simulated boundary layer velocity profile with standard law of the wall curves.

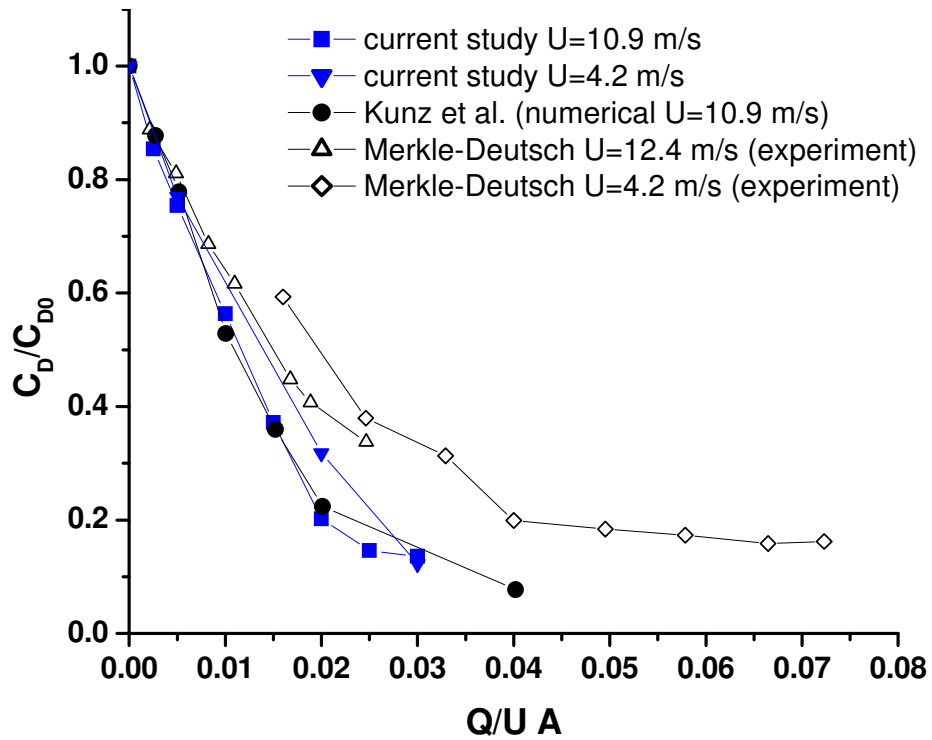


Figure 5. Comparison of the computed integrated drag coefficient with the experimental data of Merkle and Deutsch (1992) and the numerical model of Kunz et al. (2003).

To facilitate comparison of simulations with experimental study of Deutsch et al. (2003) on the influence of surface roughness on microbubble drag reduction a slightly modified computational domain was used. This domain is shown schematically in Figure 6. The dimensions of this domain were selected to closely approximate experimental conditions reported by Deutsch et al. (2003). A 127×64 grid was used for this domain. Constant velocity boundary condition was used in the domain inlet, symmetry boundary condition was used in the far field above the flat plate, no slip boundary condition is applied at the flat plate (wall 1, wall 2, wall 3, and wall 4), and constant pressure boundary condition is applied at the domain outlet. Values of  $k$  and  $\omega$  at the domain inlet were specified as  $0.001 \text{ m}^2/\text{s}^2$  and  $0.1 \text{ s}^{-1}$  respectively, which corresponds to the turbulent intensity of 0.24%. The same values were used as initial guesses for  $k$  and  $\omega$ . To compute gas inlet volumetric flow rates, the depth of the domain was assumed to be 146 mm.

Surface roughness was included in the model described above using the equivalent sand grain roughness method. In this method roughness height in inner variables is defined as

$$k_s^+ = \max\left(1.0, \frac{\rho k_s u_\tau}{\mu}\right) \quad (13)$$

Next, the value of  $\omega$  at the wall is specified as

$$\omega_w = \frac{\rho u_\tau^2}{\mu} \omega^+ \quad (14)$$

where  $\omega^+$  in the laminar sublayer is given by

$$\omega^+ = \min\left(\omega_w^+, \frac{6}{\beta_\infty^* (y^+)^2}\right), \text{ where } \omega_w^+ = \begin{cases} \left(\frac{50}{k_s^+}\right)^2 & k_s^+ < 25 \\ \frac{100}{k_s^+} & k_s^+ \geq 25 \end{cases} \quad (15)$$

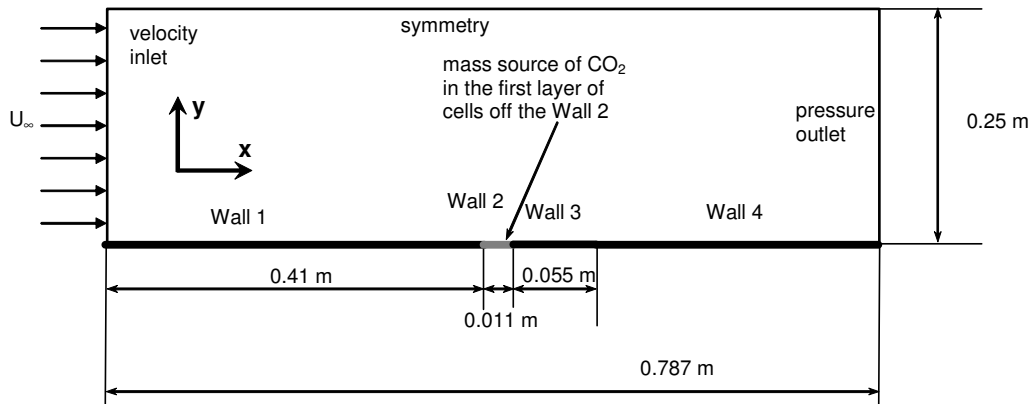


**Figure 6. Schematic diagram of the computational domain used for surface roughness effect studies.**

Simulation results were validated by comparing the results for smooth wall cases with experimental data of Deutsch et al. (2003). This comparison is shown in Figure 7, which shows integrated drag coefficient over “Wall 4” flat plate section normalized by its single-phase value as a function of the volumetric flow rate of gas injection. It is seen from the figure that computed values are very close to the data fit of experimental values. This good agreement validates our model for further studies of the influence of surface roughness.

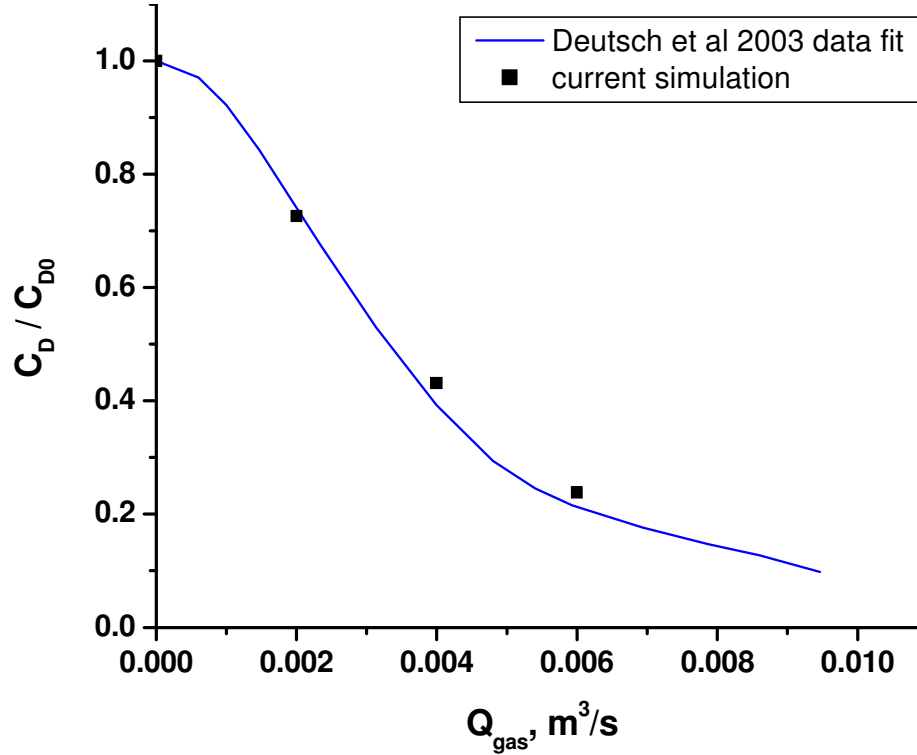


Figure 7. Comparison of the computed integrated drag coefficient for smooth wall with the experimental data of Deutsch et al. (2003).

### 3.2 MULTIPHASE MODEL

A multiphase model was used to compare predictions of standard CFD approach with Direct Numerical Simulation approach recently applied to model microbubble drag reduction. The Eulerian multiphase model was selected as it produces most accurate results among other CFD multiphase models. In this model, a multiphase flow is described as interpenetrating continua of several phases, volume fractions represent the space occupied by each phase, and the laws of conservation of mass and momentum are satisfied by each phase individually. Thus, continuity and momentum equations are solved for each phase. The Continuity equation is:

$$\frac{1}{\rho_{rq}} \left( \frac{\partial}{\partial t} (\alpha_q \rho_q) + \nabla \cdot (\alpha_q \rho_q \vec{v}_q) \right) = \sum_{p=1}^n (\dot{m}_{pq} - \dot{m}_{qp}) \quad (16)$$

where  $\rho_{rq}$  is the volume averaged density of the  $q^{\text{th}}$  phase in the solution domain.

The momentum conservation equation for a phase  $q$  is:

$$\frac{\partial}{\partial t}(\alpha_q \rho_q \bar{v}_q) + \nabla \cdot (\alpha_q \rho_q \bar{v}_q \bar{v}_q) = -\alpha_q \nabla p + \nabla \cdot \bar{\tau}_q + \alpha_q \rho_q \bar{g} + \sum_{p=1}^n (K_{pq} (\bar{v}_p - \bar{v}_q) + \dot{m}_{pq} \bar{v}_{pq} - \dot{m}_{qp} \bar{v}_{qp}) + (\bar{F}_q + \bar{F}_{\text{lift},q} + \bar{F}_{\text{vm},q}) \quad (17)$$

where  $\bar{\tau}_q = \alpha_q \mu_q (\nabla \bar{v}_q + \nabla \bar{v}_q^T) + \alpha_q \left( \lambda_q - \frac{2}{3} \mu_q \right) \nabla \cdot \bar{v}_q \bar{I}$  is the  $q^{\text{th}}$  phase stress-strain tensor;  $K_{pq} (\bar{v}_p - \bar{v}_q)$  is an interaction force between phases;  $\bar{F}_q$  is an external body force;  $\bar{F}_{\text{lift},q}$  is a lift force; and  $\bar{F}_{\text{vm},q}$  is a virtual mass force.

The lift force acting on a secondary phase  $p$  in a primary phase  $q$  is modeled after Drew and Lahey (1993) as:

$$\bar{F}_{\text{lift}} = -0.5 \rho_q \alpha_p (\bar{v}_q - \bar{v}_p) \times (\nabla \times \bar{v}_q) \quad (18)$$

The virtual mass force is encountered by accelerating secondary phase particles (or bubbles) due to the inertia of the primary phase mass. This force is computed according to Drew and Lahey (1993) as:

$$\bar{F}_{\text{vm}} = 0.5 \cdot \alpha_p \cdot \rho_q \cdot \left( \frac{d_q \bar{v}_q}{dt} - \frac{d_p \bar{v}_p}{dt} \right) \quad (19)$$

where  $\frac{d_q(\phi)}{dt} = \frac{\partial(\phi)}{\partial t} + (\bar{v}_q \cdot \nabla)\phi$  is the phase material time derivative.

To model the interaction force between phases the fluid-fluid exchange coefficient is defined as:

$$K_{pq} = \frac{\alpha_q \alpha_p \rho_p f}{\tau_p} \quad (20)$$

where  $\tau_p = \frac{\rho_p d_p^2}{18 \mu_q}$  is the particle relaxation time, and  $f$  is the drag function modeled after Schiller and Naumann (1935) as:

$$f = \frac{C_D \text{Re}}{24} \quad (21)$$

where  $\text{Re} = \frac{\rho_q |\bar{v}_p - \bar{v}_q| d_p}{\mu_q}$  is the relative Reynolds number and the drag coefficient  $C_D$  is computed as:

$$C_D = \begin{cases} 24(1 + 0.15 \text{Re}^{0.687})/\text{Re} & \text{Re} \leq 1000 \\ 0.44 & \text{Re} > 1000 \end{cases} \quad (22)$$

To satisfy the conservation of energy an enthalpy equation is solved for each phase:

$$\frac{\partial}{\partial t}(\alpha_q \rho_q h_q) + \nabla \cdot (\alpha_q \rho_q \vec{u}_q h_q) = -\alpha_q \frac{\partial p_q}{\partial t} + \overline{\tau}_q : \nabla \vec{u}_q - \nabla \cdot \vec{q}_q + \sum_{p=1}^n (\bar{Q}_{pq} + \dot{m}_{pq} h_{pq} - \dot{m}_{qp} h_{qp}) \quad (23)$$

where  $h_q$  is the specific enthalpy of the  $q^{\text{th}}$  phase,  $\vec{q}_q$  is the heat flux,  $Q_{pq}$  is the intensity of heat exchange between the  $p^{\text{th}}$  and  $q^{\text{th}}$  phases, and  $h_{pq}$  is the interphase enthalpy.

For turbulence modeling  $k$ - $\varepsilon$  turbulence model for each phase was employed. The transport equations for this model are:

$$\begin{aligned} \frac{\partial}{\partial t}(\alpha_q \rho_q k_q) + \nabla \cdot (\alpha_q \rho_q \vec{U}_q k_q) = \nabla \cdot \left( \alpha_q \frac{\mu_{t,q}}{\sigma_k} \nabla k_q \right) + (\alpha_q G_{k,q} - \alpha_q \rho_q \varepsilon_q) + \\ \sum_{l=1}^N K_{lq} (C_{lq} k_l - C_{ql} K_q) - \sum_{l=1}^N K_{lq} (\vec{U}_l - \vec{U}_q) \cdot \frac{\mu_{t,l}}{\alpha_l \sigma_l} \nabla \alpha_l + \sum_{l=1}^N K_{lq} (\vec{U}_l - \vec{U}_q) \cdot \frac{\mu_{t,q}}{\alpha_q \sigma_q} \nabla \alpha_q \end{aligned} \quad (24)$$

and

$$\begin{aligned} \frac{\partial}{\partial t}(\alpha_q \rho_q \varepsilon_q) + \nabla \cdot (\alpha_q \rho_q \vec{U}_q \varepsilon_q) = \nabla \cdot \left( \alpha_q \frac{\mu_{t,q}}{\sigma_\varepsilon} \nabla \varepsilon_q \right) + \frac{\varepsilon_q}{k_q} \left[ C_{1\varepsilon} \alpha_q G_{k,q} - C_{2\varepsilon} \alpha_q \rho_q \varepsilon_q + \right. \\ \left. C_{3\varepsilon} \left( \sum_{l=1}^N K_{lq} (C_{lq} k_l - C_{ql} K_q) - \sum_{l=1}^N K_{lq} (\vec{U}_l - \vec{U}_q) \cdot \frac{\mu_{t,l}}{\alpha_l \sigma_l} \nabla \alpha_l + \sum_{l=1}^N K_{lq} (\vec{U}_l - \vec{U}_q) \cdot \frac{\mu_{t,q}}{\alpha_q \sigma_q} \nabla \alpha_q \right) \right] \end{aligned} \quad (25)$$

where  $C_{lq} = 2$ ,  $C_{ql} = 2 \left( \frac{\eta_{lq}}{1 + \eta_{lq}} \right)$ ,  $\eta_{lq} = \frac{\tau_{t,lq}}{\tau_{F,lq}}$

To account for interphase turbulent momentum transfer, the turbulent drag term is computed as:

$$\sum_{l=1}^N K_{lq} \cdot (\vec{v}_l - \vec{v}_q) = \sum_{l=1}^N K_{lq} \cdot (\vec{U}_l - \vec{U}_q) - \sum_{l=1}^N K_{lq} \cdot \vec{v}_{\text{dr},lq} \quad (26)$$

where  $\vec{U}_l$  and  $\vec{U}_q$  are phase-weighted velocities, and  $\vec{v}_{\text{dr},lq}$  is the drift velocity for phase  $l$

defined as:  $\vec{v}_{\text{dr},lq} = - \left( \frac{D_l}{\sigma_{lq} \alpha_l} \nabla \alpha_l - \frac{D_q}{\sigma_{lq} \alpha_q} \nabla \alpha_q \right)$ .

This model captures most of the physical mechanisms that are known to be important for microbubble drag reduction phenomena such as bubble dynamics and turbulence effects. The model was solved using the FLUENT 6.2 CFD solver.

A 194 mm by 290 mm computational domain (Figure 8) with 120×120 grid points (Figure 9) was used to solve the model. The height of the computational domain was



selected so that it would be at least 20 turbulent boundary layer thicknesses, which, for the present case, was about  $\delta = 14.2$  mm at the exit of the domain. Wall-normal clustering of cells was used to resolve the boundary layer. Dimensions of the computational domain and boundary conditions are shown schematically in Figure 8. Inlet velocity profile boundary condition is used in the domain inlet, symmetry boundary condition is used in the far field above the flat plate, no slip boundary condition is applied at the flat plate, and constant pressure boundary condition is applied at the domain outlet. Inlet velocity profile was generated in a separate domain so that the turbulent boundary layer thickness is 9.7 mm with free stream velocity  $U_\infty = 0.83$  m/s. This velocity profile is shown in Figure 10 in comparison with the experimental data of DeGraaff and Eaton (2000). The simulated profile matches the experimental data reasonably well especially in the boundary layer and in close proximity to the flat plate. Values of  $k$  and  $\varepsilon$  at the domain inlet were specified as  $1.2 \cdot 10^{-5} \text{ m}^2/\text{s}^2$  and  $1.44 \cdot 10^{-8} \text{ m}^2/\text{s}^3$ , respectively. The same values were used as initial guesses for  $k$  and  $\varepsilon$ . The dimensions of the domain and the inlet velocity profile correspond to those of Direct Numerical Simulation of Ferrante and Elghobashi (2004) to facilitate comparison of the results.

To validate that the computational grid satisfied  $y^+ \leq 1$  at the first cell off the wall, the  $y^+$  at the first cell was plotted along the flat plate for all computational cases. A sample plot for the case with inlet bubble concentration  $C_v = 0.01$  is shown in Figure 11. It is seen from this figure that the condition  $y^+ \leq 1$  is satisfied for the entire surface of the flat plate. The  $y^+$  values along the flat plate for other studied cases had similar values.

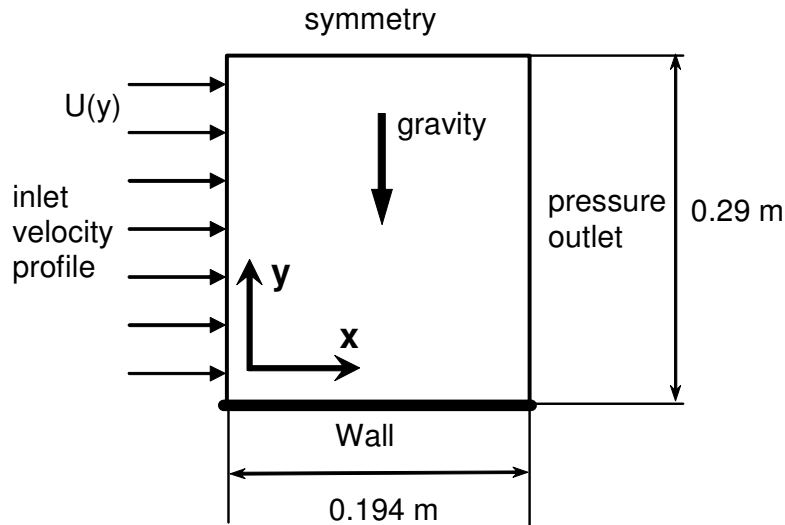


Figure 8. The computational domain used in the multiphase model.

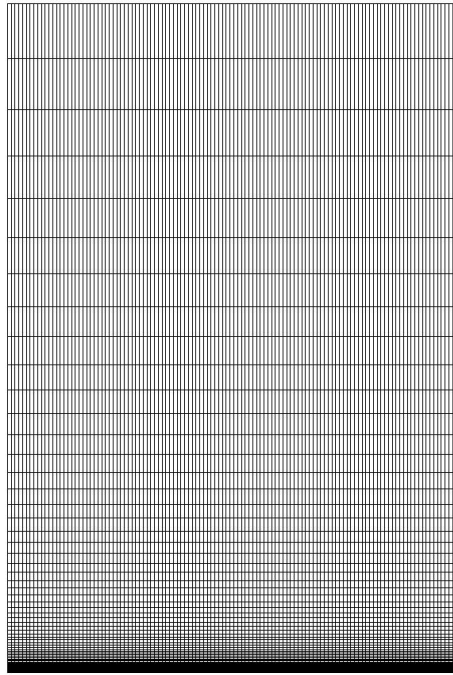


Figure 9. The 120×120 grid used in the multiphase model.

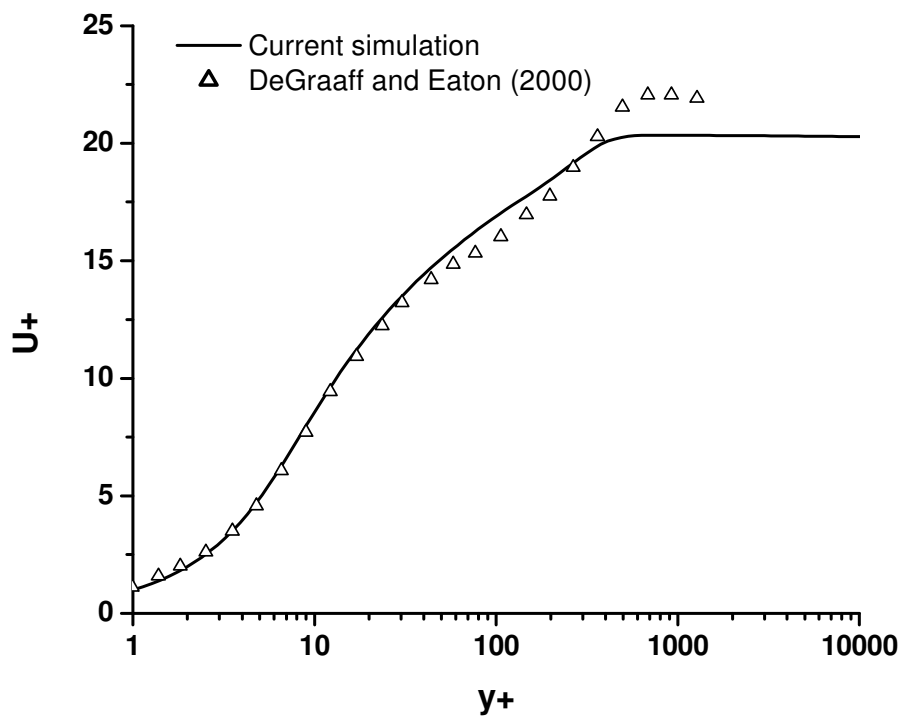


Figure 10. Inlet velocity profile used in the multiphase model.

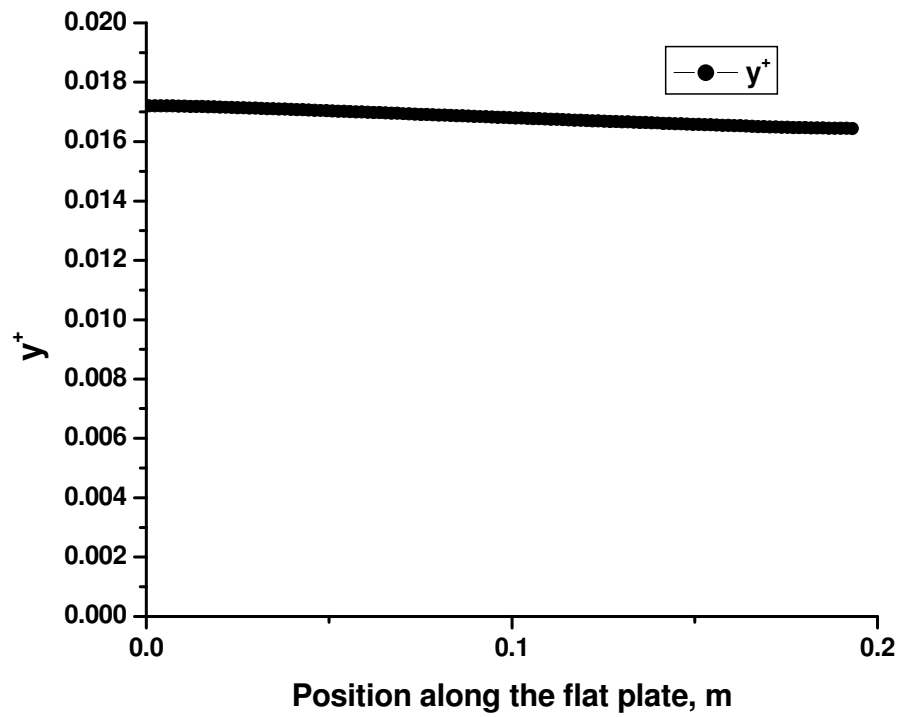


Figure 11. The  $y^+$  in the first cell of the wall along the flat plate for the  $C_v = 0.01$  multiphase model case.

## 4.0 Turbulence Intensity Effect

The effect of free stream turbulence intensity was studied by increasing turbulence kinetic energy  $k$  from  $1 \times 10^{-3} \text{ m}^2/\text{s}^2$  to  $1 \times 10^{-2} \text{ m}^2/\text{s}^2$  and then to  $7 \times 10^{-2} \text{ m}^2/\text{s}^2$ . The corresponding values of turbulence intensity are 0.24%, 0.75%, and 2%. This study was performed using the single phase model described in Section 3.1. The results of this study are shown in Figure 12 and Figure 13. It is seen from these figures that for both studied gas injection rates increasing free stream turbulence intensity results in lower drag reduction as indicated by increased value of the  $C_D/C_{D0}$ . Also Figure 13 shows that this effect is stronger for higher density ratios of water and injected gas. For example, for the density ratio of  $DR=559$ , increasing the turbulence intensity from 0.24% to 2% results in the 6.3% decrease in the drag reduction, while the same increase in the turbulence intensity for the density ratio of  $DR=125$  results in only 4.8% decrease in the drag reduction.

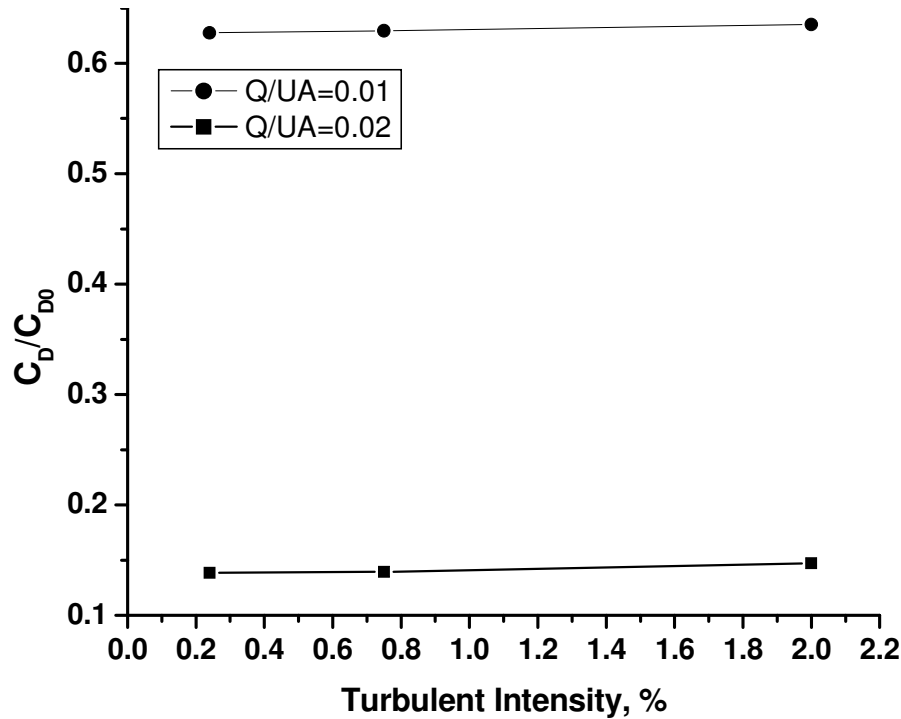


Figure 12. Free stream turbulent intensity effect on the drag reduction for different gas injection flow rates.

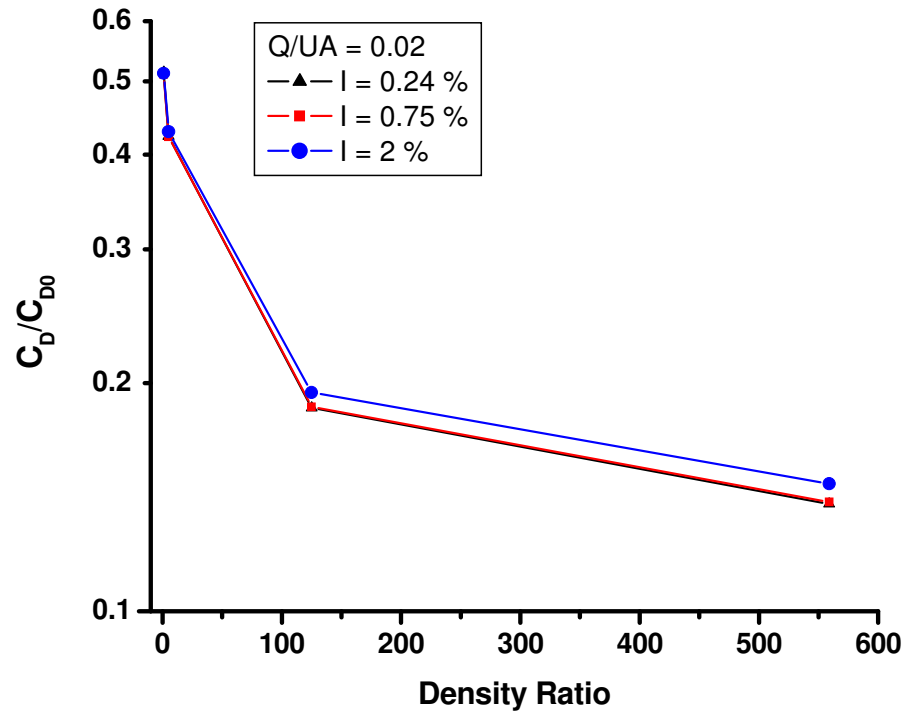


Figure 13. Free stream turbulent intensity effect on the drag reduction for different density ratios of injected gas and water ( $Q/U_{\infty}A=0.02$ ).

## 5.0 Free Stream Velocity Effect

---

The effect of free stream velocity was studied by increasing the free stream velocity from 4.2 m/s to 7.5 m/s, then to 10.9 m/s and finally to 12.4 m/s. This study was performed using the single phase model described in Section 3.1 with computational domain shown in Figure 1. Two nondimensional gas injection rates  $Q/U_{\infty}A$  of 0.01 and 0.02 were used in this study, as well as three density ratios of 5, 125, and 559. The results of the study are shown in Figure 14 and Figure 15. From Figure 14 it is seen that for both studied nondimensional gas injection rates the drag reduction increases with increasing free stream velocity as indicated by decreased value of the  $C_D/C_{D0}$ . For lower nondimensional gas injection rate, steeper increase in the drag reduction for free stream velocity increase from 4.2 m/s to 7.5 m/s is followed by a more gradual increase for free stream velocity increase from 7.5 m/s to 12.4 m/s. While approximately linear increase in the drag reduction is observed for higher nondimensional gas injection rate. Figure 15 indicates that the drag reduction is higher for higher density ratios. For example for the density ratio of DR=559 the drag reduction increased by 71% for free stream velocity increase from 4.2 m/s to 12.4 m/s, while for DR=5 the drag reduction only increased by 13% for the same free stream velocity increase.

A comparison of simulation results with the experimental data of Deutsch et al. (2003) is shown in Figure 16. The computational domain shown in Figure 6 was used for these simulations as this domain closely mimics experimental conditions of Deutsch et al. (2003). It is seen from Figure 16 that the modeling results are very close to the experimental data. Same as experiments, modeling results for fixed gas injection rate predict lower drag reduction for higher free stream velocity. It should be noted that dimensional gas injection rate is used in Figure 16, while a non-dimensional gas rate is used in Figure 14. Thus, for cases shown in Figure 14, the dimensional gas injection rate had to be adjusted for each free stream velocity to maintain fixed non-dimensional rate. Consequently, different behavior of drag reduction is observed depending on if normalization is used or not.

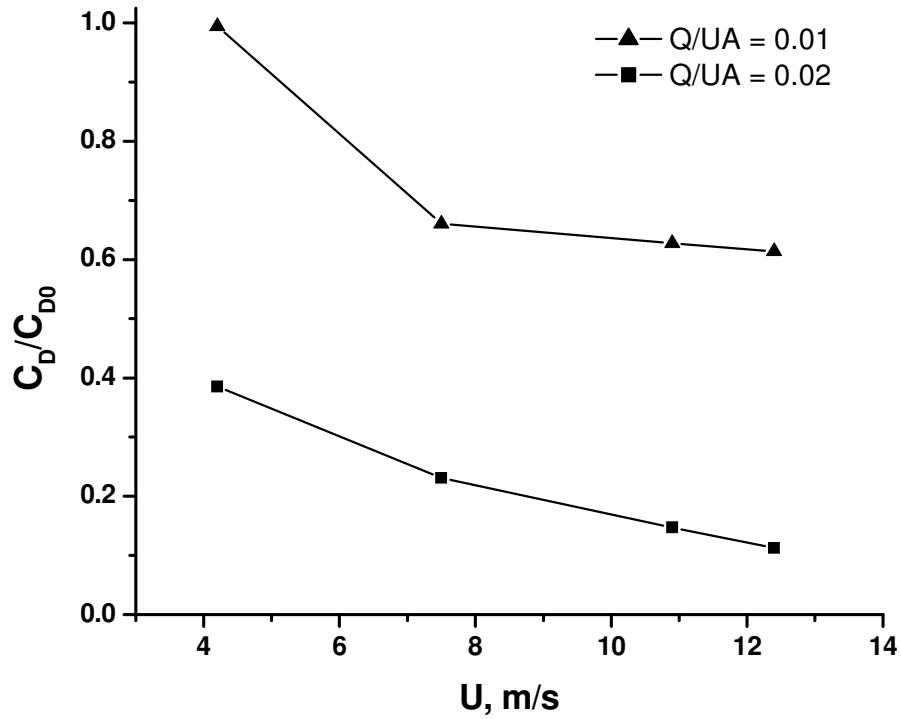


Figure 14. Free stream velocity effect on the drag reduction for different gas injection flow rates.

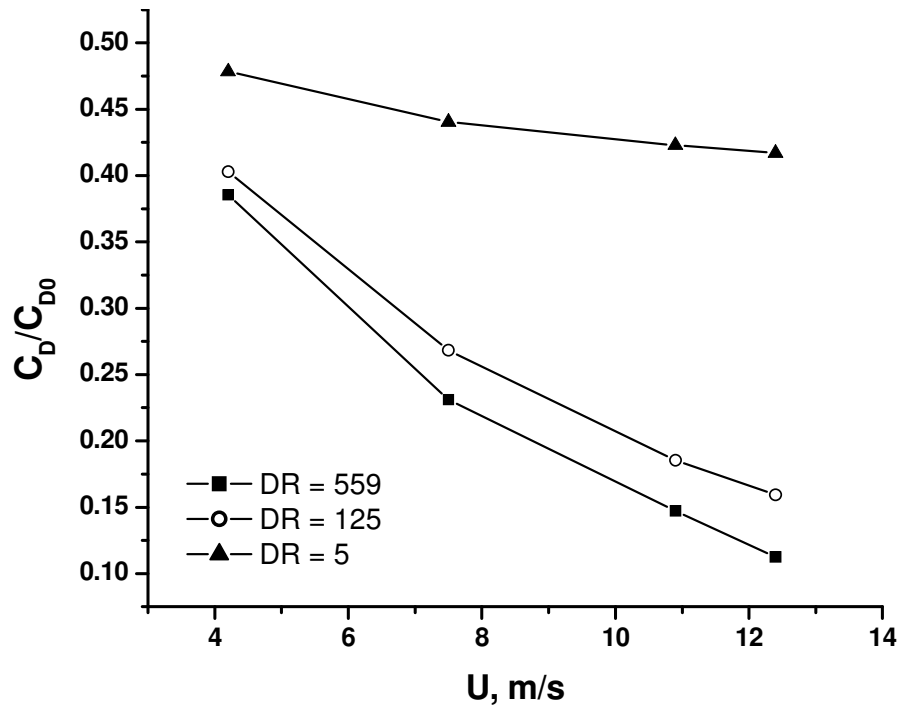


Figure 15. Free stream velocity effect on the drag reduction for different density ratios of water and injected gas ( $Q/U_{\infty}A=0.02$ ).

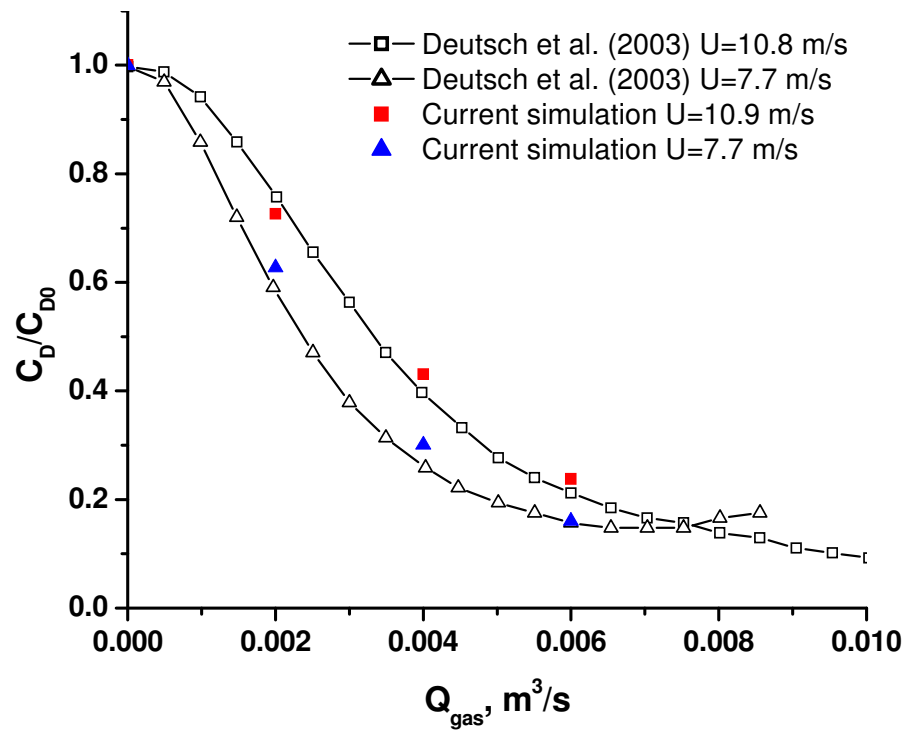


Figure 16. Comparison of numerical simulations with different free stream velocities with experimental data of Deutsch et al. (2003).



## 6.0 Surface Roughness Effect

The effect of surface roughness was studied by changing roughness height of the “Wall 4” section of the flat plate (see Figure 6), which correspond to the drag balance surface in Deutsch et al. (2003) experiments. Roughness heights  $k_s$  of 75  $\mu\text{m}$ , 150  $\mu\text{m}$  and 300  $\mu\text{m}$  were used in the simulation cases with free stream velocity of 10.9 m/s and gas injection flow rates of 0.0  $\text{m}^3/\text{s}$ , 0.002  $\text{m}^3/\text{s}$ , 0.004  $\text{m}^3/\text{s}$ , and 0.006  $\text{m}^3/\text{s}$ . This study was performed using the single phase model described in Section 3.1.

To quantify the amount of drag reduction achieved by introduction of microbubbles, the integrated drag coefficient over “Wall 4” surface for the case with bubbles was nondimensionalized by its value for the case without bubbles obtained for the same roughness height. The results are presented in Figure 17. The figure indicates that increased drag reduction is obtained with increased surface roughness for a fixed gas injection rate. The same trend was observed in experiments at the Applied Research Laboratory at Penn State (Deutsch et al. 2003).

Comparison of current numerical simulations with the experimental data of Deutsch et al. (2003) is shown in Figure 18. This figure indicates that the best agreement of numerical simulations with experiments is observed for the smooth surface. For all rough surfaces the numerical simulations over predict the drag reduction, however this over prediction reduces with increasing gas injection flow rate.

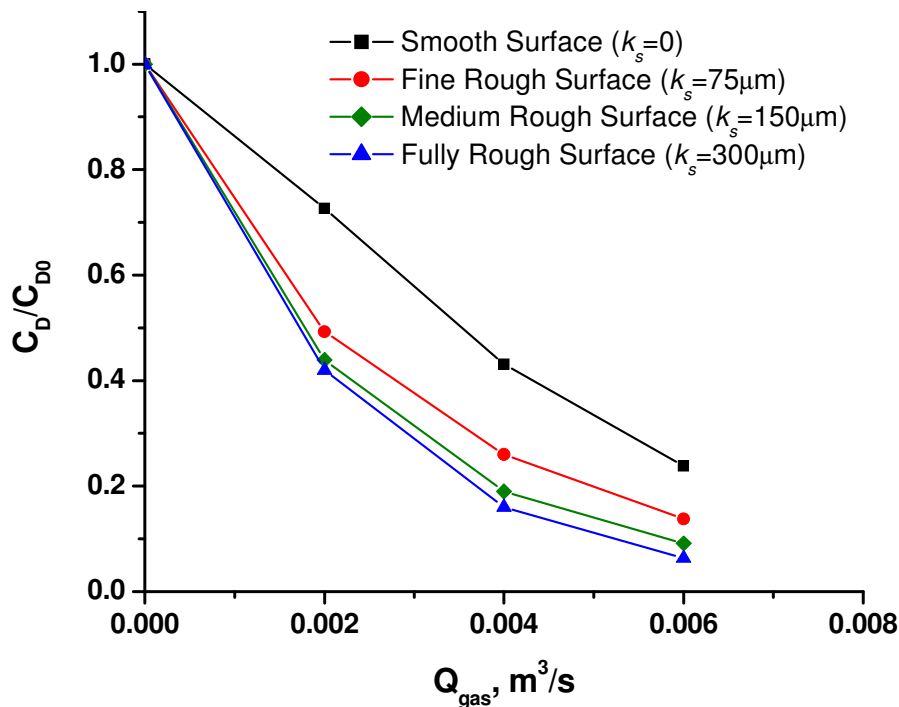


Figure 17. Surface roughness effect on the microbubble drag reduction.

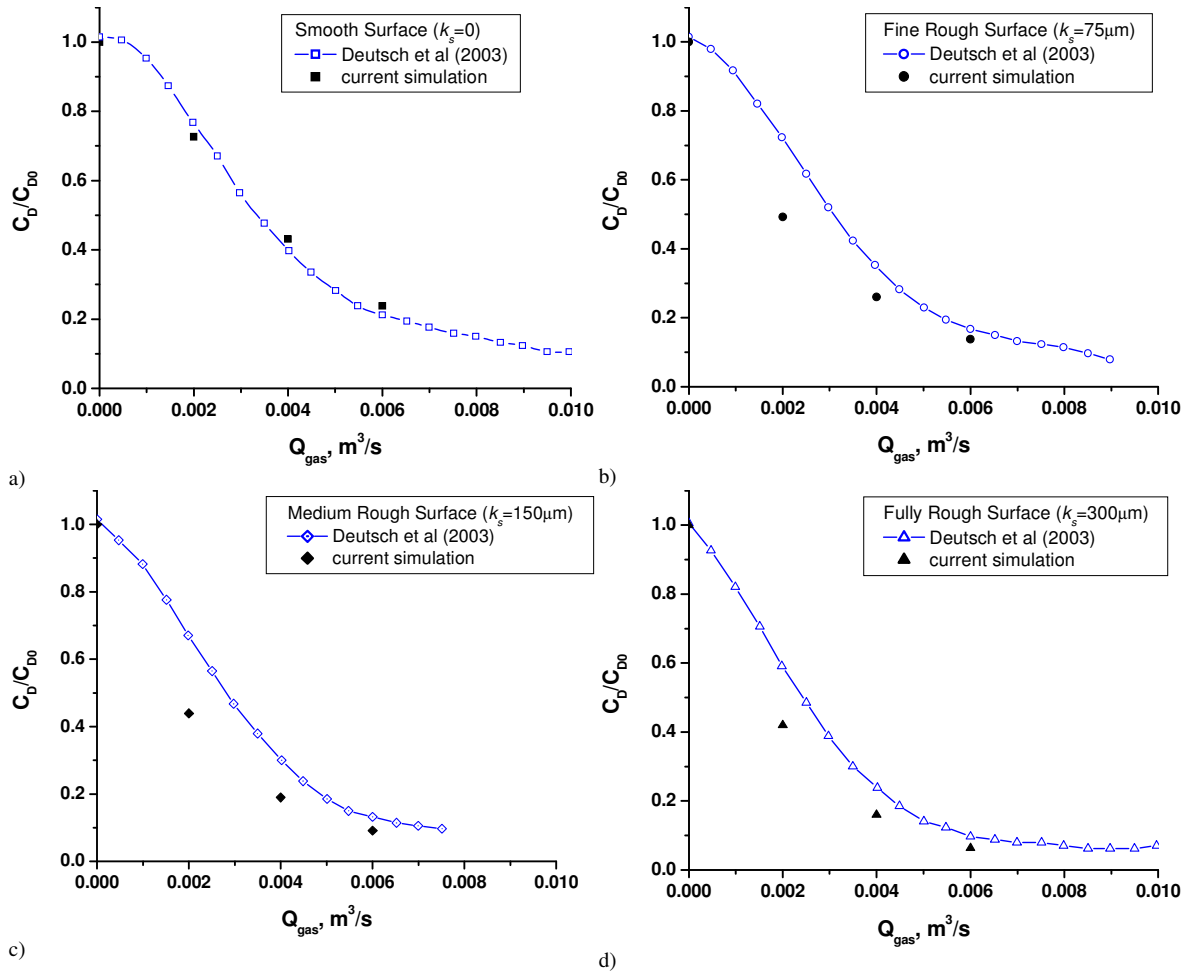


Figure 18. Comparison of numerical simulations with experimental data of Deutsch et al. (2003): a) Smooth Surface; b) Fine Rough Surface; c) Medium Rough Surface; d) Fully Rough Surface.

## 7.0 Comparison of Multiphase CFD model and DNS

---

Predictions of multiphase CFD model described in the Section 3.2 were compared with Direct Numerical Simulation results of Ferrante and Elghobashi (2004). The boundary conditions of the two approaches were matched to the best possible extent. In both simulations the free stream velocity was 0.83 m/s. The turbulent boundary layer thickness on the inlet boundary of computational domains was 9.7 mm for the both approaches. The length of both computational domains was 194 mm.

Comparison of the gas volume fraction profiles at  $x=182$  mm from the domain inlet boundary is shown in Figure 19. It is seen from the figure that the gas volume fraction profiles for the smallest studied gas concentration of  $C_v = 0.001$  are quite similar. However, at higher gas concentrations DNS predicts sharper peaks in volume fraction profiles, which are further away from the flat plate surface as compared to the CFD multiphase model prediction. The profiles obtained by the multiphase model presented here were obtained with a step function gas volume fraction boundary condition on the inlet of the computational domain. The boundary condition consisted of constant gas volume fraction inside the boundary layer and zero volume fraction above it.

An attempt was made to obtain a better match in the predicted volume fraction profiles by using gas volume fraction profile obtained by DNS model as a boundary condition on the inlet of the domain for the multiphase model. The results are shown in Figure 20. It is seen from this figure that the resulting gas volume fraction profile is similar to the one obtained with step function profile boundary condition, only peak volume fraction is higher. A sharper peak predicted by DNS was not observed for this modified boundary condition.

Since in DNS model the density of the injected gas was assumed to be zero, an attempt was made to reduce the density of the injected in our multiphase model. However, as illustrated in Figure 21 the gas volume fraction profile for the low density gas is not getting closer to the profile predicted by DNS.

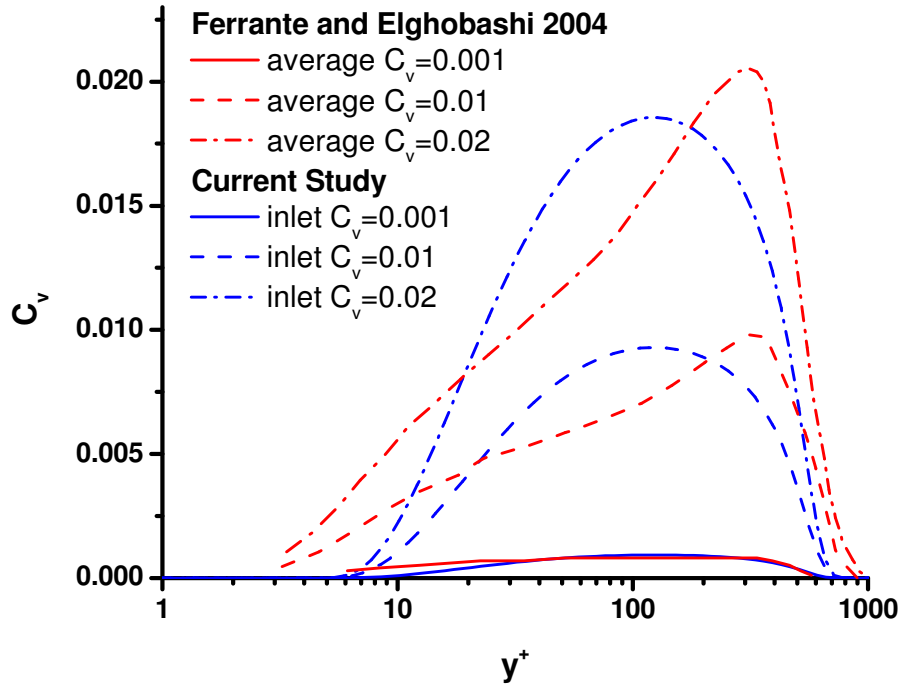
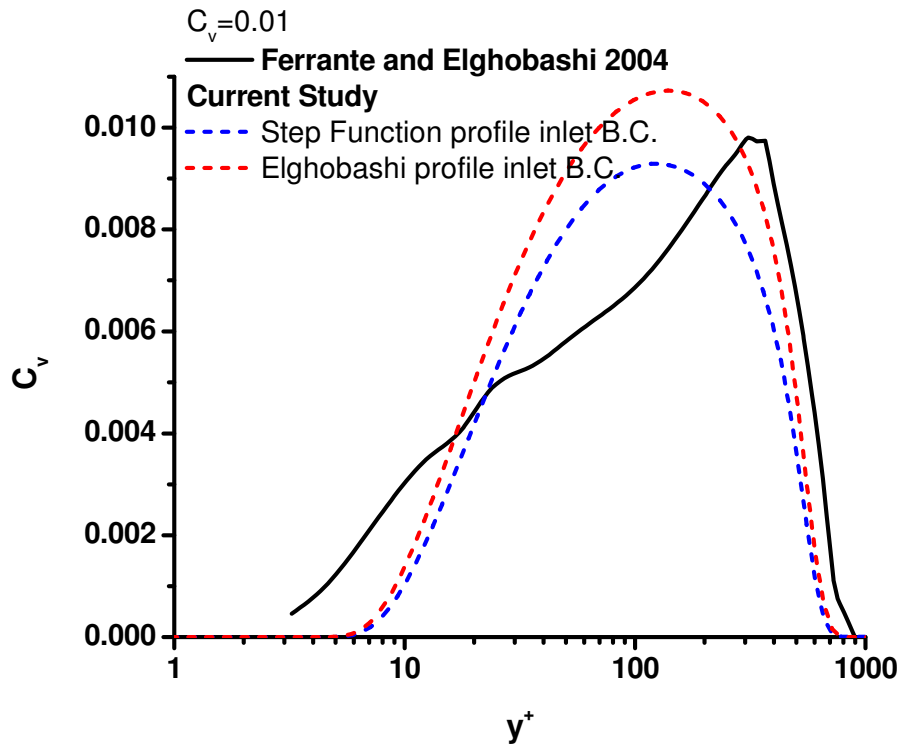
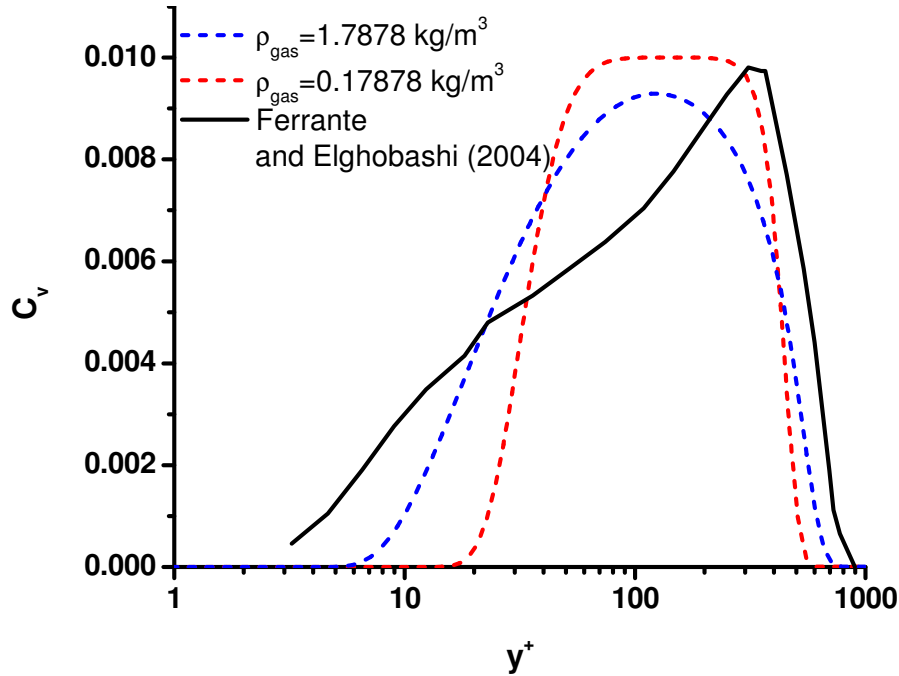
Figure 19. Gas volume fraction profiles at  $x=182$  mm.

Figure 20. Comparison of gas volume fraction profiles for different boundary conditions of the multiphase model.



**Figure 21. Comparison of gas volume fraction profiles for different injected gas density in the multiphase model.**

Comparison of the effect of the microbubbles presence on the turbulent kinetic energy (TKE) is shown in Figure 22. It is seen from this figure that the TKE predicted by the multiphase model is not affected by microbubbles presence, while DNS predicts decrease in the TKE peak as well as shifting of this peak away from the flat plate surface. It is worth noting that the multiphase model predicts TKE peak location at the same distance from the flat plate as DNS prediction for the case with microbubbles.

Comparison of the drag reduction predicted by the two models is shown in Figure 23. On this figure the drag reduction is represented as a ratio of the integrated drag coefficients over the flat plate surface with and without bubbles in the flow. It is seen from the figure that the drag reduction predicted by the multiphase model is substantially lower than that predicted by the DNS model. It is also seen that gas volume fraction profile used as the boundary condition on the domain inlet for the multiphase model has little effect on the predicted drag reduction. This is indicated in the figure by practically coinciding lines for the step function profile and the one obtained from DNS results.

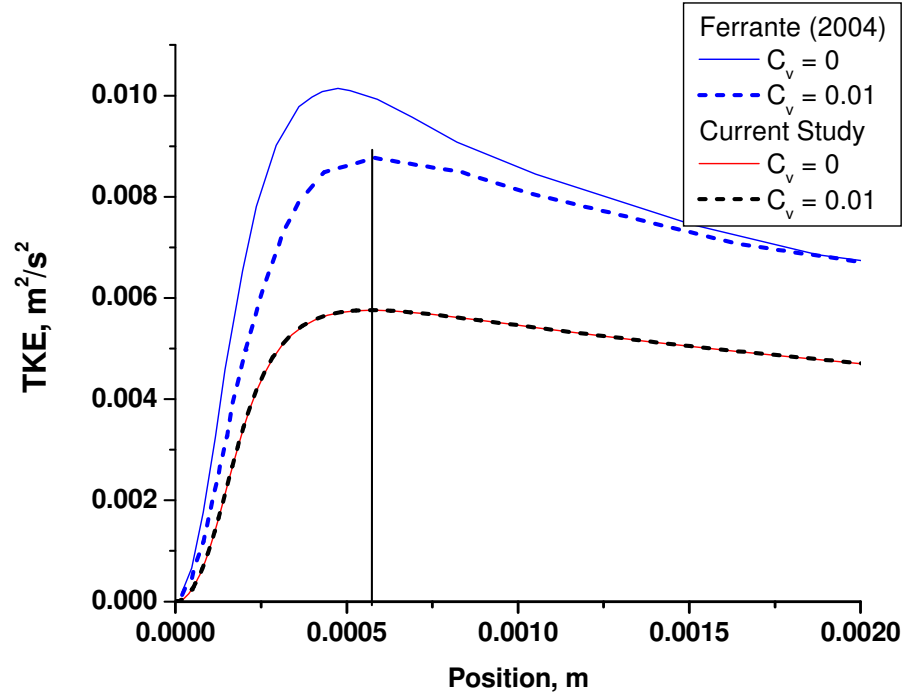


Figure 22. Microbubble effects on the Turbulent Kinetic Energy.

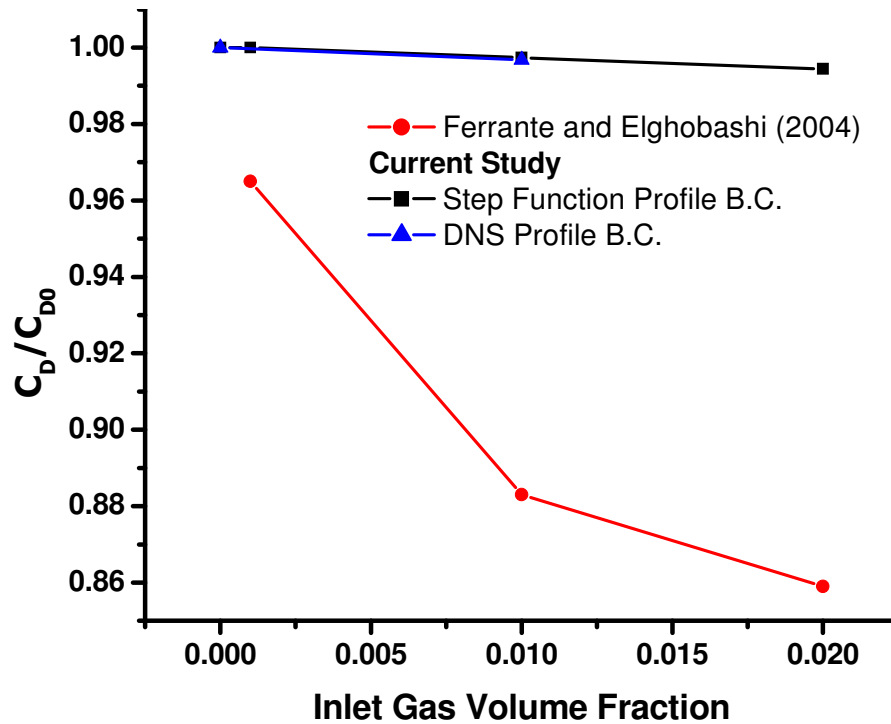


Figure 23. Comparison of the drag reduction predicted by the multiphase CFD and DNS models.

Ferrante and Elghobashi (2004) reported gas concentration as the average volume fraction of bubbles in the computational domain. However, in the beginning of their computation all bubbles were randomly distributed inside the boundary layer. This leads to bubbles volume fraction in the boundary layer to be 3.7 times higher than the average volume fraction in the domain. We have performed simulations for gas volume fractions in the boundary layer which are 3.7 times higher than the average volume fractions reported in the DNS modeling (e.g. we used  $C_v = 0.0037; 0.037; 0.074$  and instead of  $C_v = 0.001; 0.01; \text{ and } 0.002$  respectively). The drag reduction predicted in these simulations is compared with DNS model in Figure 24. Compared to Figure 23, the drag reduction obtained with higher volume gas fractions is closer to that predicted by DNS, but the difference is still as high as 7%. Additionally, when these higher concentrations are used, the gas volume fraction profiles differ significantly from those predicted by DNS, as shown in Figure 25.

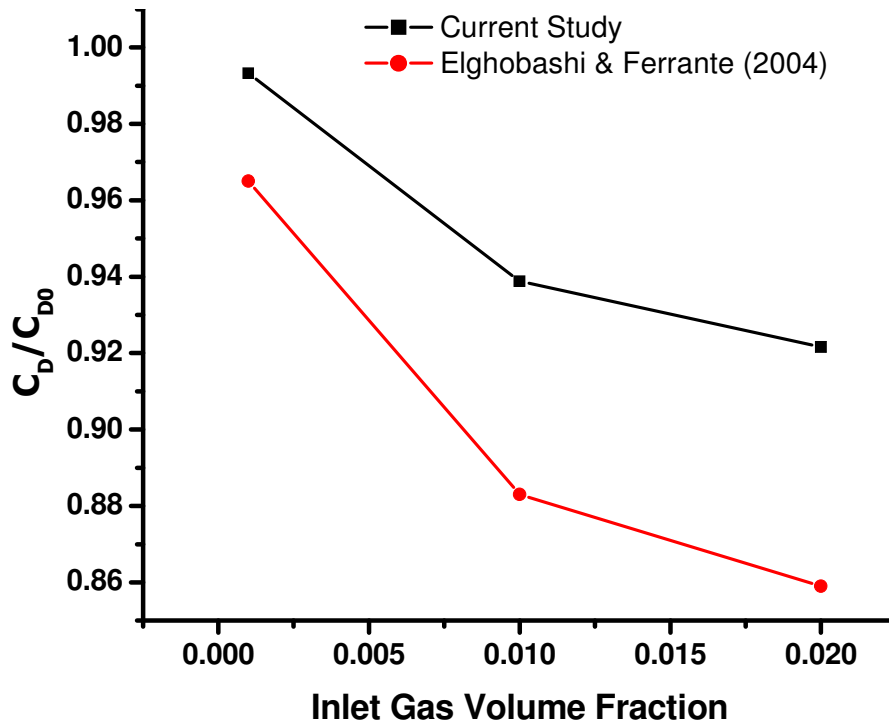


Figure 24. Comparison of the drag reduction predicted by the multiphase CFD model with gas volume fractions increased 3.7 times and DNS model.

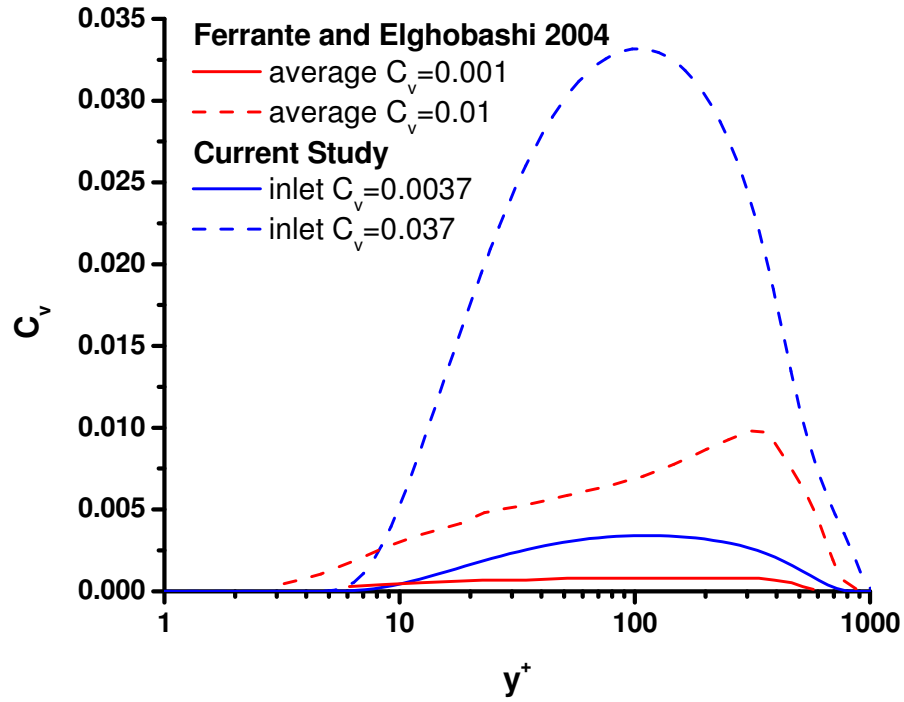


Figure 25. Comparison of gas volume fraction profiles predicted by the multiphase CFD model with gas volume fractions increased 3.7 times and DNS model.



## 8.0 Conclusions

---

Major conclusions from the performed parametric numerical simulation study are summarized below:

- Increased free stream turbulence intensity results in lower drag reduction, and this effect is stronger for higher density ratios of water and injected gas
- For the same free stream velocity increase, the drag reduction is higher for higher density ratio
- For fixed gas injection rate, lower drag reduction is predicted for higher free stream velocity, which is in a good agreement with experimental observations
- For a fixed gas injection rate, increased drag reduction is obtained with increased surface roughness, which is also in a good agreement with experimental observations
- Good quantitative agreement was observed between the simulations with the single phase model and experimental data of Deutsch et al.(2003)
- Gas volume fraction and turbulent kinetic energy profiles predicted by the multiphase model were similar but not identical to those predicted by the Direct Numerical Simulation of Ferrante and Elghobashi (2004)
- The drag reduction predicted by the multiphase model was substantially lower than that predicted by the DNS model of Ferrante and Elghobashi (2004)

## 9.0 Publications Stemming from this Research

---

P.V. Skudarnov and C.X. Lin, Density Ratio And Turbulence Intensity Effects In Microbubble Drag Reduction Phenomenon, FEDSM2005-77075, 2005 ASME Fluids Engineering Division Summer Meeting and Exhibition, Houston, TX, USA, June 19-23, 2005.

P.V. Skudarnov and C.X. Lin, Drag Reduction by Gas Injection into Turbulent Boundary Layer: Effect of Surface Roughness, Int. J. Heat and Fluid Flow, to be submitted, 2006.

## Acknowledgement

Research team members of this project are grateful to Dr. Robert F. Kunz of ARL Penn State for guidance, helpful discussions, and encouragement throughout the entire project duration.

## Nomenclature

	Symbols
A	Area, m <sup>2</sup>
C <sub>D</sub>	Integrated drag coefficient, dimensionless
DR	$= \frac{\rho_{water}}{\rho_{gas}}$ Density ratio, dimensionless
k <sub>s</sub>	roughness height, m
p	Pressure, Pa
Q	Flow rate, m <sup>3</sup> /s
Re	Reynolds number, dimensionless
t	Time, s
U <sub>∞</sub>	Free-stream velocity, m/s
u <sub>i</sub>	mean velocity components (i = 1, 2, 3), m/s
u' <sub>i</sub>	fluctuating velocity components (i = 1, 2, 3), m/s
u <sub>τ</sub>	$= \sqrt{\frac{\tau_w}{\rho}}$ friction velocity, m/s
u <sup>+</sup>	$= \frac{u}{u_\tau}$ velocity in inner variables, dimensionless
y	wall normal coordinate, m
y <sup>+</sup>	$= \frac{\rho u_\tau y}{\mu}$ wall normal coordinate in inner variables, dimensionless
μ	Dynamic viscosity, Pa-s
ρ	Density, kg/m <sup>3</sup>
τ <sub>w</sub>	wall shear stress, Pa

## References

- DeGraaff, D. and Eaton, J. (2000). Reynolds-number scaling of the flat-plate turbulent boundary layer. *J. Fluid Mech.* 422, 319–346.
- Deutsch, S., Moeny, M., Fontaine, A., and Petrie, H. (2003). Microbubble Drag Reduction in Rough Walled Turbulent Boundary Layers. 4<sup>th</sup> ASME–JSME Joint Fluids Engineering Conference, Honolulu, Hawaii, July 6–11, 2003, Paper N FED2003-45647.
- Drew, D. A. and Lahey, R. T. (1993) In *Particulate Two-Phase Flow*, Butterworth-Heinemann, Boston, pp. 509-566.
- Ferrante, A., and Elghobashi, S. (2004). On the physical mechanisms of drag reduction in a spatially developing turbulent boundary layer laden with microbubbles. *Journal of Fluid Mechanics.* 503, 345-355.
- Happel, J., and Brenner, H. (1965). *Low Reynolds Number Hydrodynamics*. Prentice Hall, Inc., Englewood Cliffs, NJ, pp. 438-443.
- Kim, S.-Y., and Cleaver, J.W. (1995). The persistence of drag reduction following the injection of microbubbles into a turbulent boundary layer. *International Communications in Heat and Mass Transfer*, 22(3), 353-357.
- Kunz, R.F., Deutsch, S., and Lindau, J.W. (2003). Two Fluid Modeling of Microbubble Turbulent Drag Reduction. 4<sup>th</sup> ASME–JSME Joint Fluids Engineering Conference, Honolulu, Hawaii, July 6–11, 2003, Paper N FED2003-45640.
- Kunz, R.F. (2003). Private Communication.
- Legner, H.H. (1984). A simple model for gas bubble drag reduction. *Physics of Fluids*, 27(12), 2788-2790.
- Madavan, N.K., Merkle, C.L., and Deutsch, S. (1985). Numerical investigations into the mechanisms of microbubble drag reduction. *Journal of Fluids Engineering*, 107, 370-377.
- Marie, J.L. (1987). Simple Analytical Formulation For Microbubble Drag Reduction. *PhysicoChemical Hydrodynamics*, 8(2), 213-220.
- McCormick, M.E., and Bhattacharya, R. (1973). Drag reduction of a submersible hull by electrolysis. *Naval Eng. J.*, 85, 11-16.
- Meng, J.C.S., and Uhlman, J.S., Jr. (1998). Microbubble formation and splitting in a turbulent boundary layer for turbulence reduction. *Proceedings of the International Symposium on Seawater Drag Reduction*, 22-23 July 1998, 341-355.
- Merkle, C.L., and Deutsch, S. (1992). Microbubble Drag Reduction in Liquid Turbulent Boundary Layers. *Applied Mechanics Reviews*, 45(3), 103-127.
- Schiller L. and Naumann Z. (1935). *Z. Ver. Deutsch. Ing.*, 77:318.
- Wilcox, D.C. (1998). *Turbulence Modeling for CFD*. DCW Industries, Inc., La Canada, California.
- Xu, J., Maxey, M.R., and Karniadakis, G.E. (2002). Numerical simulation of turbulent drag reduction using micro-bubbles. *Journal of Fluid Mechanics*, 468, 271-281.

REPORT DOCUMENTATION PAGE				Form Approved OMB No. 0704-0188	
Public reporting burden for this collection of information is estimated to average 1 hour per response, including the time for reviewing instructions, searching existing data sources, gathering and maintaining the data needed, and completing and reviewing this collection of information. Send comments regarding this burden estimate or any other aspect of this collection of information, including suggestions for reducing this burden to Department of Defense, Washington Headquarters Services, Directorate for Information Operations and Reports (0704-0188), 1215 Jefferson Davis Highway, Suite 1204, Arlington, VA 22202-4302. Respondents should be aware that notwithstanding any other provision of law, no person shall be subject to any penalty for failing to comply with a collection of information if it does not display a currently valid OMB control number. <b>PLEASE DO NOT RETURN YOUR FORM TO THE ABOVE ADDRESS.</b>					
1. REPORT DATE (DD-MM-YYYY) 31-03-2006		2. REPORT TYPE Final		3. DATES COVERED (From - To) July 2004 - December 2005	
4. TITLE AND SUBTITLE  Assessments of Bubble Dynamics Model and Influential Parameters in Microbubble Drag Reduction				5a. CONTRACT NUMBER N00014-04-1-0717	
				5b. GRANT NUMBER	
				5c. PROGRAM ELEMENT NUMBER	
6. AUTHOR(S)  Skudarnov, P. V.; Lin, C. X.				5d. PROJECT NUMBER	
				5e. TASK NUMBER	
				5f. WORK UNIT NUMBER	
7. PERFORMING ORGANIZATION NAME(S) AND ADDRESS(ES)  Florida International University Tamiami Campus 115 Primera Casa Miami, FL 33199				8. PERFORMING ORGANIZATION REPORT NUMBER  ARC-2004-M023-001-04	
9. SPONSORING / MONITORING AGENCY NAME(S) AND ADDRESS(ES) Office of Naval Research Ballston Centre Tower One 800 North Quincy Street Arlington, VA 22217-5660				10. SPONSOR/MONITOR'S ACRONYM(S)	
				11. SPONSOR/MONITOR'S REPORT NUMBER(S)	
12. DISTRIBUTION / AVAILABILITY STATEMENT  Approved for Public Release; Distribution is Unlimited.					
13. SUPPLEMENTARY NOTES					
14. ABSTRACT During the course of this research effort computational parametric studies of the microbubble drag reduction phenomena were conducted. The effects of mixture density variation, free stream turbulence intensity, free stream velocity, and surface roughness on the microbubble drag reduction were studied using a single phase model based on Reynolds-averaged Navier-Stokes transport equations. Additionally, predictions of Eulerian multiphase model for microbubble laden flow were compared with Direct Numerical Simulation from the open literature.					
15. SUBJECT TERMS Microbubbles, Turbulent boundary layer, Drag reduction					
16. SECURITY CLASSIFICATION OF:			17. LIMITATION OF ABSTRACT	18. NUMBER OF PAGES  35	19a. NAME OF RESPONSIBLE PERSON Peter Skudarnov
a. REPORT	b. ABSTRACT	c. THIS PAGE			19b. TELEPHONE NUMBER (include area code) 305-348-2377